Nanoscale

PAPER

View Article Online
View Journal | View Issue

Cite this: *Nanoscale*, 2026, **18**, 3387

A novel method for rapidly functionalizing perovskite oxides

Weiwei Fan, *[a] Zhu Sun*[b] and Rui Xiao[a]

Received 29th November 2025,
Accepted 1st January 2026

DOI: 10.1039/d5nr05033b

rsc.li/nanoscale

High-performance perovskite oxides are instrumental in catalytic processes and energy conversion. The exsolution of metallic nanoparticles from perovskite oxide hosts to form metal/oxide heterogeneous catalysts provides unprecedented opportunities for manipulating the catalytic activity of perovskites. Herein, we design and demonstrate a new approach to rapidly trigger exsolution and tune the electrochemical performance of perovskites. We show that by applying pulsed thermal shock several times (~50 ms pulse width) and voltage shock for ~40 s, exsolution-based products can be prepared on a timescale of seconds. With an increase in the number of pulses, the particle density increases first due to an increase in the concentration of oxygen vacancies that can serve as nucleation sites and then reaches a threshold governed primarily by the content of exsolvable metal atoms in the host lattice. Owing to the additionally generated active sites and conducting paths for active species, perovskite activity is significantly improved, thus eventually yielding a prominent enhancement in electrochemical performance.

Introduction

ABO_3 perovskite, a class of materials that share a particular crystal structure similar to that of the naturally existing mineral perovskite $CaTiO_3$, is a good candidate for energy conversion, energy storage and catalysis.[1–5] In an ideal cubic perovskite structure, the larger A cation (A^{m+}) coordinated by 12 oxygen anions is located at the corners of the cube, the smaller B cation (B^{n+}) octahedrally coordinated by six oxygen anions is at the center of the cube, and the oxygen anions (O^{2-}) are located at the center of each cube face. By changing the environmental conditions or doping,[6–8] the perfect cubic structure undergoes various distortions, such as rotation (lowering the symmetry of the crystal from cubic to other phases, like orthorhombic or rhombohedral, and allowing for flexibility to accommodate various-sized cations), octahedral tilting, A- and B-site ordering (A or B sites can have an ordered arrangement of different cations), cation off-centering, and oxygen vacancies (affecting surface chemistry, catalytic activity and conductivity), eventually endowing a wide range of functional properties.[9–12]

Owing to these characteristics, perovskite oxides are widely used as electrodes for solid oxide fuel cells (SOFCs), which can convert chemical energy to electrical energy in an environmentally friendly manner.[10,13–17] Since catalysis primarily takes place on the surface of the electrode catalyst during cell operation,[18–20] it is of great significance to modify the surface of the perovskite oxide to offer more active sites,[21,22] thus improving the eventual catalytic activity. Conventionally, infiltration or deposition (like chemical vapor deposition and atomic layer deposition) methods are broadly applied to deposit nanoparticles on the surface of target perovskites for fabricating a heterogeneous catalyst with a nanoparticle/support structure.[23–27] However, the troublesome issues of high cost, interminable procedures, long preparation cycle and inferior stability of the product make it urgent to develop alternative techniques. As an emerging approach, exsolution has been built and rapidly developed in the past few years.[28–31] Different from conventional methods that prepare nanoparticle/support products in an *ex situ* way, nanoparticles can be produced on the surface of perovskite supports *in situ* by applying the exsolution method.[32] Briefly, by providing a driving force, exsolvable metal atoms with high catalytic activity can be drained out of the host lattice during exsolution. Moreover, nanoparticle/support products prepared by applying the exsolution method usually show good stability and distribution due to their anchored property.[33–38]

In principle, the exsolution of particles from a perovskite support is a type of phase segregation that is generally induced by chemical gas reduction.[39,40] Due to the weak driving force (chemical potential, $\mu = \mu^0 + RT\ln(P/P^0)$) provided to the system and low kinetics of cation diffusion, it usually takes tens of hours to acquire nanoparticle-modified perovskite using traditional methods. Moreover, the particle density is generally low because of the fallow surface of the host for par-

[a]*Key Laboratory of Energy Thermal Conversion and Control of Ministry of Education, School of Energy and Environment, Southeast University, 2 Dong Nan Da Xue Road, Nanjing, 211189, China. E-mail: fanww@seu.edu.cn*
[b]*School of Materials Science and Engineering, Shanghai Jiao Tong University, 800 Dongchuan Road, Shanghai, 200240, China*

ticle nucleation, severely underestimating the effectiveness of exsolution in boosting the activity of the perovskite oxide. Given that the exsolution characteristics have a close relationship with the local environment of active transition metal atoms in the perovskite host, there stands a good chance to tune the exsolution kinetics by releasing lattice oxygen since it can make the metal cation nearby more exsolvable. Moreover, after the oxygen release, the introduced point defect of the oxygen vacancy could potentially serve as a nucleation site and hence accelerate the exsolution process as well as manipulate the particle density, eventually producing an exsolution-based perovskite with high catalytic activity.

With the aim of rapidly triggering exsolution and tailoring the electrochemical activity of the perovskite electrode for SOFC, in this study, we propose a novel technique of pulsed thermal shock and voltage shock (Fig. 1), named the P–V shock technique for convenience. Briefly, $La_{0.32}Ca_{0.48}Ti_{0.94}Ni_{0.06}O_{3-\delta}$ (LCTN) perovskite was applied as the model material. It was found that after pulsed thermal shock at ~1600 °C for several numbers (~50 ms in pulse width) and voltage shock at 2 V for ~40 s, exsolution could be successfully triggered in a timescale of seconds. Moreover, the oxygen vacancy concentration and particle density can be well manipulated by altering the pulse number of the thermal shock. Consequently, the electrochemical activity of the LCTN perovskite electrode was effectively improved at the working temperatures.

Exsolution triggered by P–V shock

Considering that Ti-based oxides generally show good structural stability within a wide oxygen partial pressure (pO_2) window, and the introduction of other elements with a lower valence state can alter the perovskite's properties,[41] in this work, $La_{0.32}Ca_{0.48}Ti_{0.94}Ni_{0.06}O_{3-\delta}$ (LCTN) oxide was synthesized using the solid-state reaction method. Meanwhile, the design and introduction of an A-site deficiency into the host lattice is mainly because it can generally endow dynamical exsolution when treating the host oxide. This is primarily because the concentration of BO Schottky defects (Fig. S1) can be well tuned by introducing an A-site deficiency, accelerating the migration of lattice oxygen and generating metallic nanoparticles (eqn (1) and (2)). A home-made setup was designed and built to conduct the P–V shock. During the pulsed thermal shock, carbon paper (60 × 10 × 1 mm) was selected and applied as the heating source, and ~20 A current was supplied to the system to provide a temperature of ~1600 °C in a N_2 atmosphere. The pulse width was set to 50 ms. Subsequently, voltage shock was carried out at 2 V for ~40 s at 800 °C in N_2.

$$B_B^{\times} + O_O^{*} \leftrightarrow BO + V_O^{\cdot\cdot} + V_B^{''} \quad (1)$$

$$BO \leftrightarrow B + \frac{1}{2}O_2 \quad (2)$$

The P–V shock was conducted by gradually increasing the pulse number (PN) of the pulsed thermal shock. When the PD

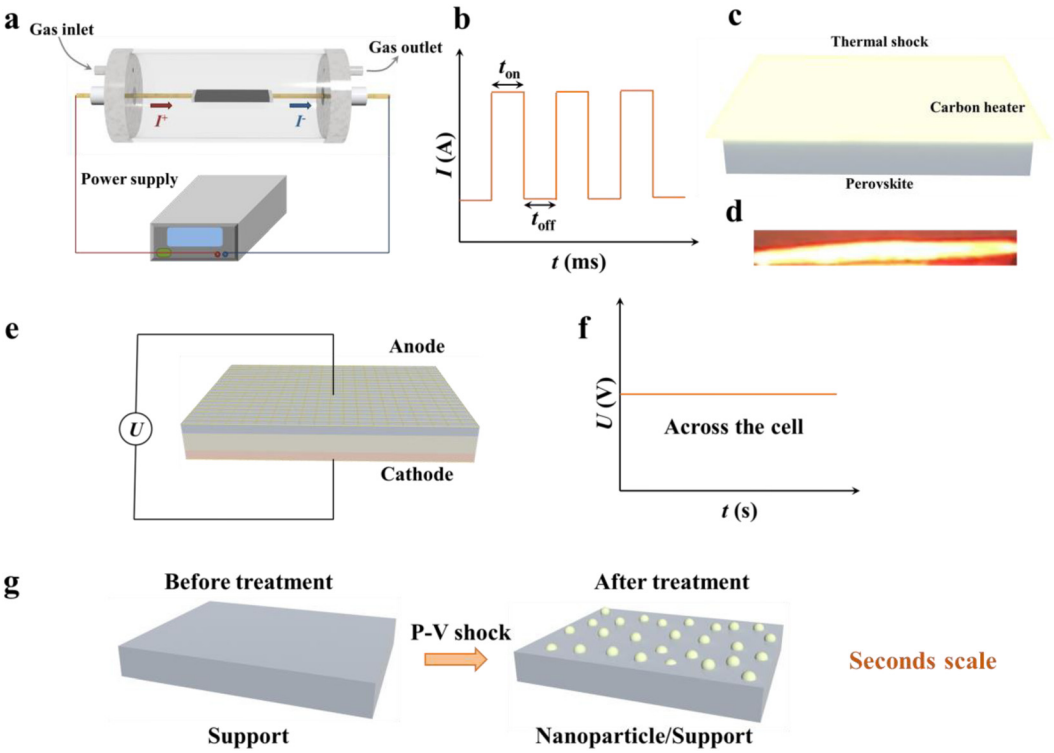

Fig. 1 (a) Schematic of the pulsed thermal shock setup. (b) Current profile as a function of time for pulsed thermal shock. (c) Schematic of the pulsed thermal shock treatment. (d) Captured picture of the pulsed thermal shock during the treatment. (e) Schematic of the voltage shock treatment. (f) Voltage profile as a function of time for the voltage shock. (g) Illustration of perovskite before and after the P–V shock treatment.

was 3, surprisingly, it was found that a small number of nanoparticles with an average particle size of 14 ± 3 nm (Fig. S1) appeared on the surface of the LCTN host (Fig. 2a), indicating that exsolution was successfully triggered by applying the P–V shock technique. As a reference, the LCTN was treated individually using voltage shock. However, the results showed that no observable particles were detected (Fig. S2), suggesting that the exsolution phenomenon was a result of the synergistic effect of the pulsed thermal shock and voltage shock.

In general, the eventual catalytic activity of a perovskite oxide has an intimate relationship with the number of exsolved particles (particle density), so we naturally consider whether the particle density could be tuned by altering the pulse number. Then, a P–V shock was carried out by gradually increasing the PN at an interval of 3. Interestingly, when PN was increased from 3 to 6, the particle density varied from 4 to 29 μm^2 after the P–V shock (Fig. 2a and Fig. S1). Moreover, when PN increased to 9, the particle density prominently increased to 86 particles μm^2, suggesting that one could prospectively manipulate the exsolution degree by altering PN (Fig. 2b). Here, it should be noted that when PN was further increased to 12, the particle density (83 particles μm^2) did not change significantly, implying that there was a threshold for exsolving nanoparticles from the host. In principle, for a certain perovskite solid solution, there should exist a solubility window $[c_1, c_2]$ for the active dopant. For example, when the doping level is in $[c_1, c_2]$, a solid solution with a single phase can be successfully obtained. However, when the doping level exceeds the $[c_1, c_2]$ window, impurity phases are generated during solid solution formation. Therefore, it is probably rational to attribute the threshold phenomenon of the particle density during exsolution to the limited concentration of the active dopant (Fig. 2d). In other words, as the exsolution proceeds, the surface becomes barren of exsolvable atoms, which in turn limits the exsolution degree during the P–V shock. In addition, the exsolution depth was roughly estimated, and the results showed that with an increase in pulsed thermal shock numbers, the exsolution depth increased from ~2 to 43 nm (Fig. 2e), further suggesting that the exsolution degree can be effectively tuned by applying the P–V shock.

To obtain more information about the exsolution triggered by the P–V shock, the concentration of oxygen vacancy $V_O^{\cdot\cdot}$ was

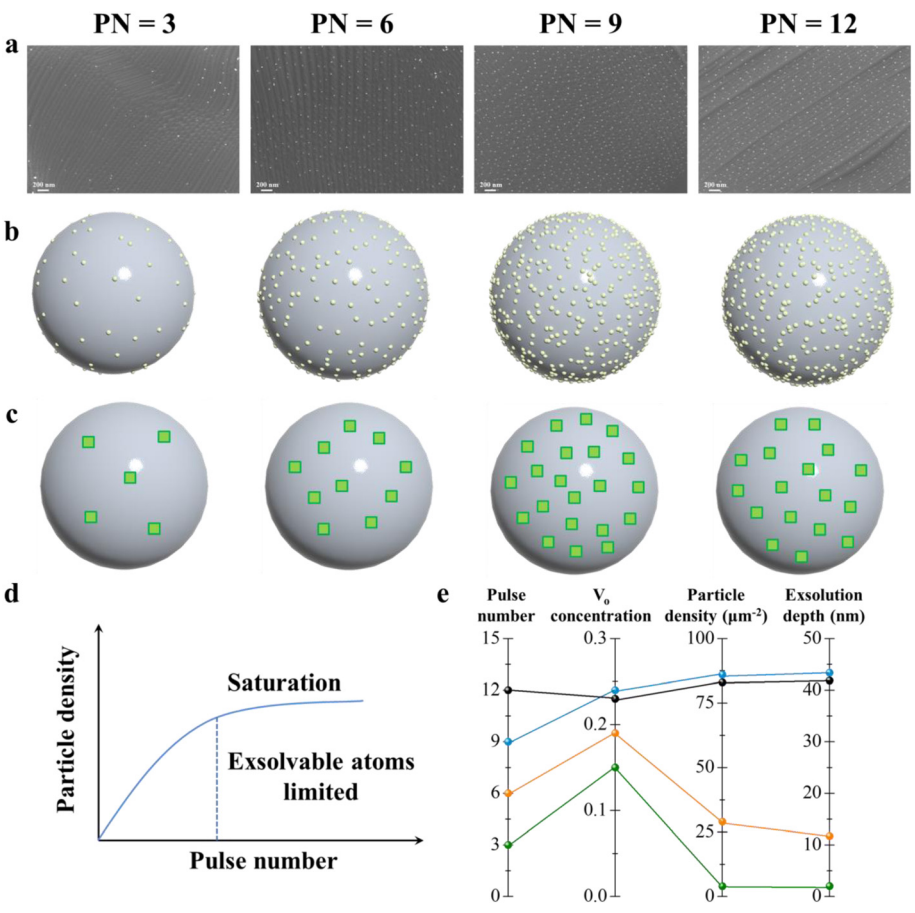

Fig. 2 (a) SEM images of the LCTN perovskite after P–V shock. (b) Illustration of the effect of the pulse number on the particle density. (c) Illustration of the effect of the pulse number on the concentration of oxygen vacancy (as depicted by the green rectangle); PN represents the pulse number. (d) Diagram of the relationship between particle density and pulse number. (e) Variation of oxygen vacancy concentration, particle density and exsolution depth as a function of the pulse number.

investigated by applying the iodometric titration method. For credibility, three parallel experiments were conducted, and the average value was adopted for the analysis. For the sake of clarity, we refer to the as-synthesized LCTN as pristine LCTN and the LCTN treated by 3 pulse numbers, 6 pulse numbers, 9 pulse numbers and 12 pulse numbers as PN3, PN6, PN9 and PN12, respectively. The results showed that for the pristine LCTN, an oxygen vacancy concentration C_V of 0.12 ± 0.03 was obtained. Interestingly, as the pulse number increased, the C_V first increased and then varied slightly, showing a variation trend similar to that of the particle density (Fig. 2b and c). For example, C_V values of 0.15 ± 0.02, 0.19 ± 0.03, 0.24 ± 0.02 and 0.23 ± 0.02 were acquired for PN3, PN6, PN9 and PN12 samples, respectively. From the viewpoint of defect chemistry, point defects, such as oxygen vacancies, generated on the surface of the perovskite host can provide sites for nucleation due to the decreased barrier energy, as shown in the latter section, facilitating the formation of nanoparticles. Actually, it has been demonstrated that the nucleation of Au nanoclusters preferably takes place at the oxygen vacancies of the TiO_2 substrate.[42] Thus, by changing the pulse number, the population of exsolved particles can be effectively tuned. In addition, it was found that for all cases, the average particle size was similar. In principle, the thermodynamically equilibrating size of a particle is closely associated with the kinetics of the particle growth. Therefore, according to the experimental results, it might be reasonable to deduce that all the samples exhibited a similar growth behavior during the P–V shock. For comparison, LCTN was also treated by applying a conventional gas reduction method (900 °C 20 h in H_2), and the results showed that only a few particles with large sizes were generated (Fig. S3), suggesting slow exsolution kinetics, which might be ascribed to the intrinsically inert surface. In other words, the P–V shock technique could trigger an exsolution of higher quality.

Crystal structure of the LCTN

To verify the crystal structure of the as-synthesized LCTN, XRD was conducted on LCTN powders; then, Rietveld refinement was carried out based on the collected profile. It was found that the recorded XRD pattern could be well indexed according to an orthodromic structure (Fig. S4) with lattice parameters of a = 5.4723 (3) Å, b = 7.7275 (2) Å and c = 5.4698 (3) Å, which belonged to the space group of *Pbnm* (62) (Fig. 3a). Microstructurally, the B-site transition metals Ti/Ni with smaller ionic radius ($r_{Ti^{4+}}$ = 74.5 pm and $r_{Ni^{2+}}$ = 69 pm) sit at the centers of octahedrons that are surrounded by oxygen atoms, and these BO_6 octahedrons are periodically arranged along the a, b and c axes, while the A-site metals La/Ca with larger ionic radius ($r_{La^{3+}}$ = 106 pm and $r_{Ca^{2+}}$ = 114 pm) are filled in the space among the octahedrons (Fig. 3b). Overall, the LCTN perovskite solid solution with a single phase was successfully prepared in this study.

Moreover, the XRD profile of the LCTN perovskite after P–V shock was collected (Fig. 3c). In comparison, it can be found that in addition to the primary diffraction peaks of the LCTN

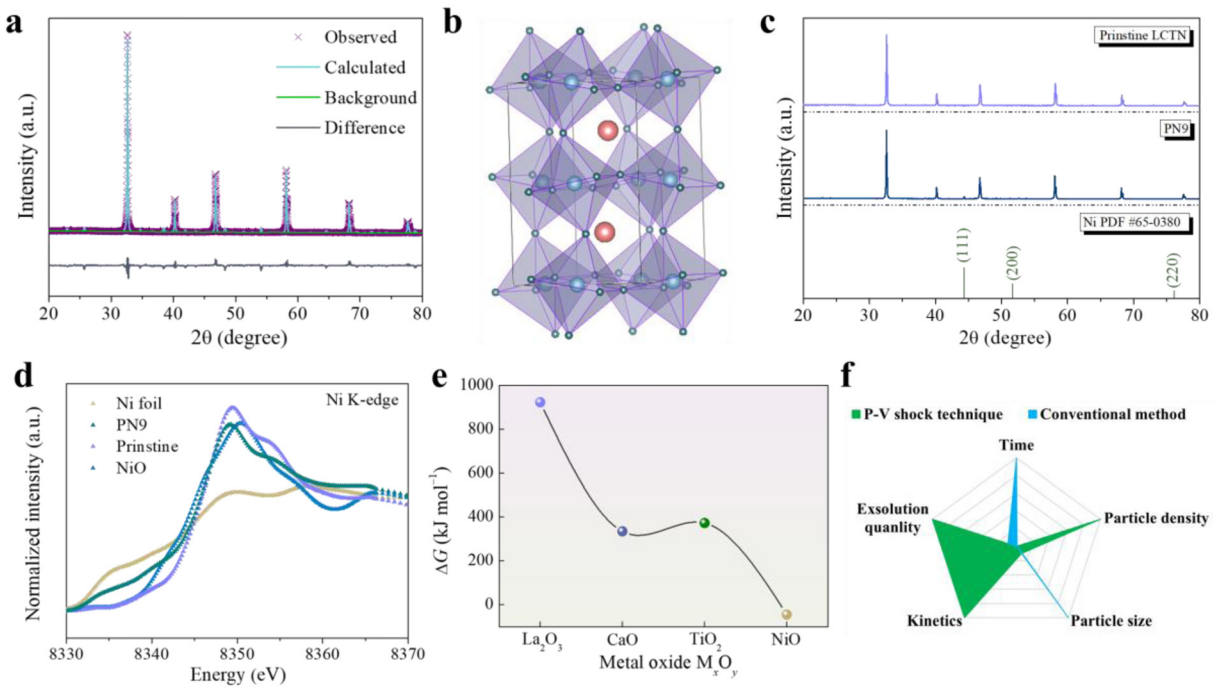

Fig. 3 (a) Rietveld refinement XRD profile of the as-synthesized LCTN. (b) Crystal structure of the LCTN, where pink spheres denote La/Ca, blue spheres denote Ti/Ni, and green spheres denote O. (c) XRD profiles of LCTN before and after the P–V shock. (d) Normalized Ni K-edge XANES for PN9. (e) Gibbs free energy values of reducing the corresponding oxides to metals at 800 °C. (f) Comparison of exsolution properties between the P–V shock technique and the conventional method.

phase, an extra diffraction peak appeared at the 2θ of ~44° for the P–V shocked LCTN, which could be most probably attributed to the Ni phase, as indicated in the Ni PDF (#65-0380), suggesting that exsolution of Ni nanoparticles occurred during the P–V shock (eqn (1)). Actually, a similar phenomenon was also observed by other researchers.[43] Furthermore, XANES was conducted on the LCTN after P–V shock. As expected, the collected results further confirmed the generation of Ni^0 (Fig. 3d). After a quantitative analysis by a linear combination fitting, it was found that 26% Ni^0 was produced, and an average oxidation state of +1.48 was acquired. In fact, a negative Gibbs free energy value of −46.47 kJ mol^{-1} can be obtained for the reduction of NiO to Ni (Fig. 3e). In other words, in comparison with other metal oxides, NiO is more prone to be reduced during treatment. In sum, the formation of abundant zero-valent nanoparticles can be rapidly (second-level scale) realized by applying the P–V shock technique. Additionally, compared to those of the conventional method, the P–V shock technique shows faster exsolution kinetics, higher particle density and smaller particle size. For example, a higher exsolution quality can be obtained by applying the P–V shock technique (Fig. 3f).

$$La_{0.32}Ca_{0.48}Ti_{0.94}Ni_{0.06}O_{3-\delta} \rightarrow La_{0.32}Ca_{0.48}Ti_{0.94}Ni_{0.06-x}O_{3-\delta-y} + Ni_x + y/2O_2 \quad (3)$$

Mechanism of exsolution triggered by pulsed thermal shock and voltage shock

In view of the validity of the P–V shock technique to trigger the exsolution of nanoparticles from the perovskite host and combined with the experimental results, a possible mechanism is proposed. As demonstrated by previous studies,[42,44] an oxygen vacancy plays a key role in mediating exsolution. Given the underlying thermodynamic principles, the creation of an oxygen vacancy in a certain oxide involves breaking chemical bonds and removing an atom from its lattice site. This requires a certain amount of energy, known as oxygen vacancy formation energy (E_f). The concentration of an oxygen vacancy (C_V) in a crystal at a given temperature (T) can generally be described using the following Arrhenius equation:

$$C_V = N \times e^{\frac{-E_f}{k_B T}}, \quad (4)$$

where N is the number of potential oxygen sites in the crystal, k_B is the Boltzmann constant, and T is the absolute temperature in Kelvin.

Therefore, the relationship between oxygen vacancy concentration and temperature is direct and exponential. As the temperature of the system increases, the equilibrium concentration of the oxygen vacancies also increases exponentially. This is because the formation of a vacancy is an endothermic process that becomes more thermodynamically favorable at increased temperatures. This is different from the conventional way in which lattice oxygen is removed using a furnace to provide a driving force. Restricted by the related heating elements, the heating rate and heating temperature provided are generally low, resulting in long-term treatment and weak kinetics of oxygen vacancy formation. In this study, we proposed to apply carbon paper to provide a driving force; only ~1 s was needed so that the system could be rapidly increased up to ~1600 °C. At this high-level temperature, thermal energy overcomes the vacancy formation energy, which causes a rapid release of oxygen atoms from their lattice positions, thus increasing the total concentration of vacancies that can preferentially serve as nucleation sites during exsolution. Hence, owing to the strong driving force, removal of oxygen in the LCTN perovskite lattice and generation of oxygen vacancy (eqn (5)) took place dynamically during pulsed thermal shock until reaching a new thermodynamic equilibrium state (Fig. 4a and b), consequently giving rise to the pre-activation of LCTN. Actually, experimental results showed that compared to that of pristine LCTN, a 2 times enhancement of oxygen vacancy concentration was achieved for LCTN after pulsed thermal shock for 9 times.

$$O_O^{\times} \leftrightarrow V_O^{\bullet\bullet} + 2e^- + 1/2O_2(g) \quad (5)$$

During the following voltage shock (~40 s) to the pre-activated perovskite (Fig. 4c and d), numerous electrons (e^-) were injected into the system, leading to a dynamical reduction in the transition metal with high reducibility; for example, the Gibbs free energy for reducing NiO to metallic Ni at 800 °C is about −46.47 kJ mol^{-1}. In virtue of the pre-generated oxygen vacancies, the kinetics of the reduction process would be enhanced, due to which the escape of lattice oxygen could bring about the isolation of the transition metal to maintain the primitive structure. At the initial stage, the nickel cations Ni^{2+} existing in the first few layers of the LCTN surface diffuse to the top surface driven by the electrical potential built between them. Then, the nickel cations are dynamically reduced to zero-valent metal atoms Ni^0 ($Ni^{2+} + 2e^- \rightarrow Ni^0$). Subsequently, the nucleation that preferentially occurs at the place where surface point defects, like oxygen vacancy, exist to minimize the total surface free energy. Then, the generated Ni atoms as a feeding source move to the clusters nearby, resulting in particle growth until reaching the thermodynamically equilibrium size. As the voltage shock proceeds, the nickel cations existing in the deeper area are drained out and then undergo similar procedures, as described previously. Based on the experimental results, for a certain perovskite oxide, there exists a threshold depth for exsolving the active metal cations from the lattice. In other words, a barrier zone of exsolvable metal cations is formed after voltage shock (Fig. 4e), leading to a threshold of particle density. To acquire a higher particle density, more driving force should be supplied to the system to drain out the active metal cations existing beyond the barren zone.

In general, exsolution can produce additional active sites, thus lowering the barrier energy of the dissociative adsorption of gas molecules. Moreover, during the formation of metallic nanoparticles, oxygen vacancies are generated to follow the rule of charge neutrality. In principle, the chemical potential that can serve as a driving force to modulate the migration of

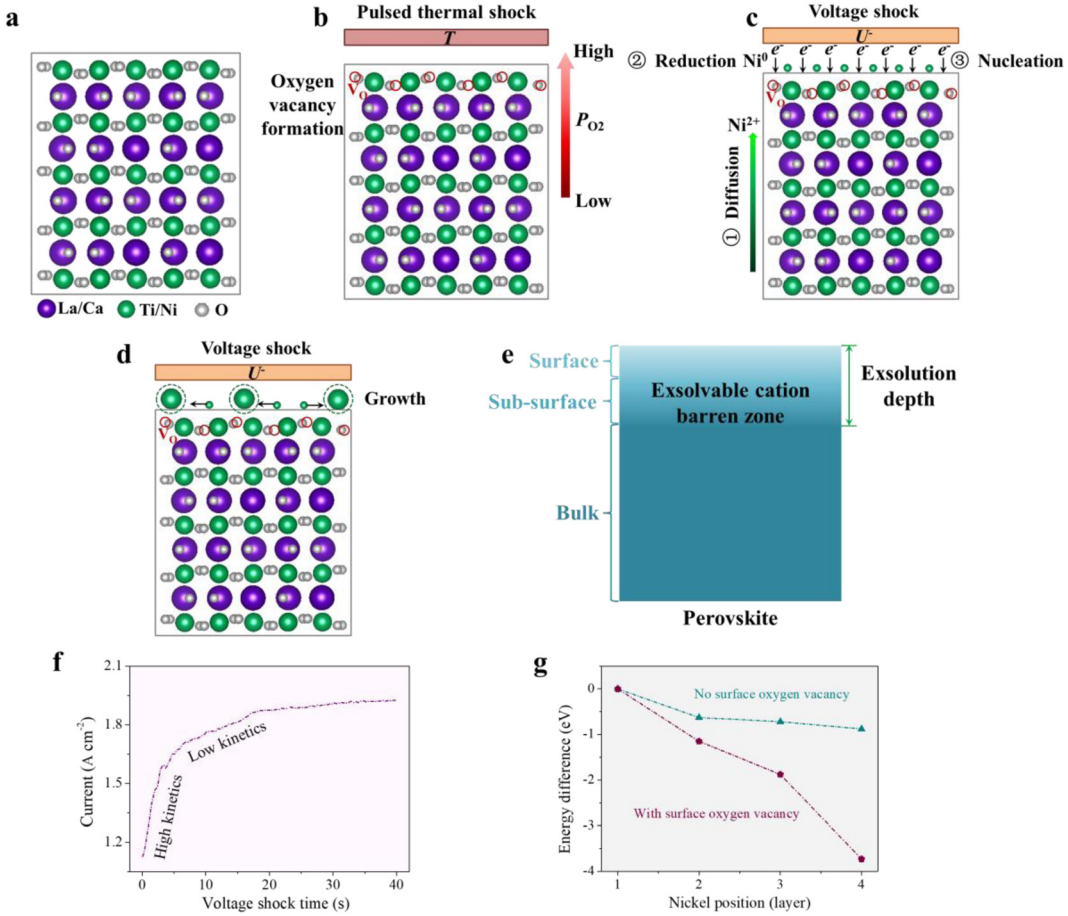

Fig. 4 (a) Crystal structure of LCTN perovskite. Purple spheres represent La/Ca, green spheres represent Ti/Ni and grey spheres represent O. (b) Illustration of oxygen vacancy formation during pulsed thermal shock. (c and d) Illustration of exsolution processes during voltage shock. (e) Schematic of exsolution limited by the exsolvable metal cation in the sub-surface. (f) Cell current as a function of time during voltage shock. (g) Energy difference with respect to nickel position and surface oxygen vacancy availability.

oxygen anions has an intimate connection with the oxygen vacancies, generally following $\mu_O = \mu_O^0 + (RT/2)\ln pO_2$. Thus, the additionally formed oxygen vacancies can provide more pathways for oxygen anion migration, which further influences the O^{2-} flux and the consumption amount of O_2 reactant in unit time. Synergistically, the exsolved active metal nanoparticles and the concurrently formed oxygen vacancies can enhance the kinetics of relative electrochemical reactions. Furthermore, since the surface generally possesses a large free volume, which is beneficial for the steps of nucleation and growth, it shows faster kinetics of particle generation (Fig. 4f). In principle, atom stability can be estimated by segregation energy. Thus, the energy difference between nickel with a surface oxygen vacancy and without a surface oxygen vacancy was estimated by a pair potential-based simulation. It was found that reduced nickel energy could be obtained by introducing an oxygen vacancy (Fig. 4g), resulting in enhanced stability. Actually, similar behavior was also observed by other researchers.[45] Thus, owing to the additional generated oxygen vacancies during the pulsed thermal shock, enhanced exsolution can be expected. In a word, exsolution kinetics can be efficiently tuned by oxygen releasing, and the nanoparticle-decorated material can be obtained in a timescale of seconds by applying the P–V shock technique.

Electrocatalytic activity of the P–V shocked LCTN

In order to investigate the electrocatalytic activity of the LCTN perovskite before and after the P–V shock, electrochemical impedance spectroscopy (EIS) was collected in a frequency range of 10^5–10^{-1} Hz at different temperatures under open-circuit voltage (OCV) conditions after stabilization. The results showed that, similar to the pristine LCTN (Fig. S5), a polarization resistance (R_p) of 49.4 Ω cm^2 was obtained at 650 °C, while it decreased to 6.4 Ω cm^2 at 800 °C. This reduction of R_p was mainly due to the enhanced kinetics of the electrode reaction at elevated temperatures, namely thermal activation enhanced electrochemical performance. These high polarization resistances indicate the low activity of the pristine LCTN on electrochemically oxidizing hydrogen.

Interestingly, similar to PN3, lower R_p values were acquired during the operation, and the R_p value varied from 21.3 Ω cm^2 at 650 °C to 3.3 Ω cm^2 at 800 °C (Fig. 5a), suggesting an

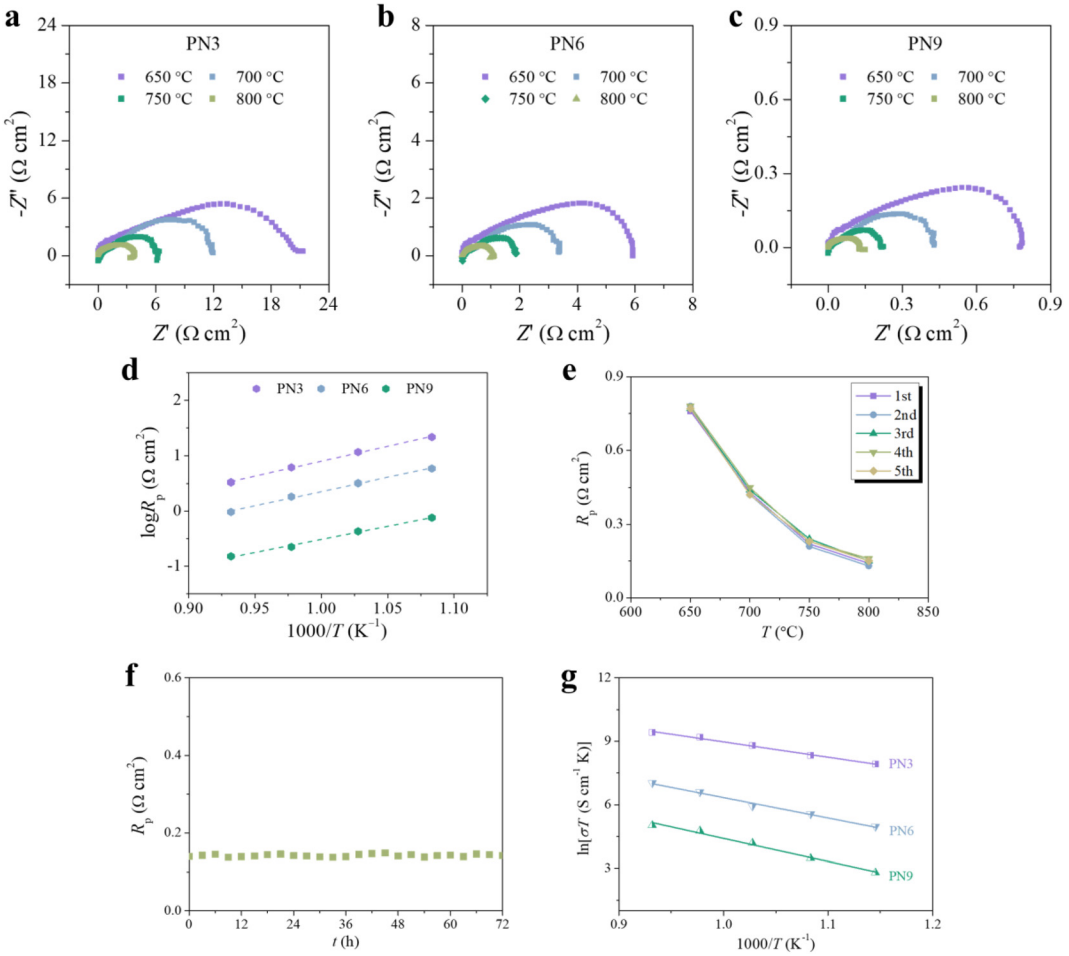

Fig. 5 Nyquist plots of (a) PN3, (b) PN6 and (c) PN9 under OCV at different temperatures. (d) Arrhenius plots of R_p of PN3, PN6 and PN9. (e) Thermal cycling performance of PN9. (f) Profile of R_p as a function of time at 800 °C for PN9. (g) Electrical conductivity of PN3, PN6 and PN9 at different temperatures in hydrogen.

improvement in electrochemical activity. This was primarily attributed to the P–V shock treatment since the exsolved Ni nanoparticles with high activity could accelerate the reaction of hydrogen oxidation. As expected, a further decrease in R_p value took place for both PN6 and PN9 (Fig. 5b and c). For example, the R_p rapidly decreased to 0.1 Ω cm^2 for PN9 at 800 °C, deriving from the numerously generated active sites that were beneficial for the corresponding electrochemical reaction. Generally, the electrochemical reaction takes place at the triple-phase boundary (TPB) where the gas reactant, electrons and active ions concurrently meet. By applying P–V shock, the additionally generated pathways for the migration of these species can extend the TPB length, thus decreasing the polarization resistance and enhancing the electrochemical activity. Overall, P–V shock is an effective technique for tuning the electrochemical activity of perovskites.

In order to obtain more information about the electrochemical performance of the pristine and P–V shocked LCTN, activation energy (E_a), relating to the processes of diffusion, adsorption, dissociation, and charge transfer, was calculated using the following equation:

$$R_p = A \exp\left(-\frac{E_a}{k_B T}\right), \quad (6)$$

where A is the pre-exponential factor, k_B is the Boltzmann constant and T is the absolute temperature. E_a can be acquired by calculating the slope of the plot depicted by $\log R_p$ *vs.* $1/T$. After a careful calculation, it was found that the E_a value was 1.16 ± 0.03 eV for the pristine LCTN (Fig. S6), while it decreased to 1.07 ± 0.01, 1.01 ± 0.02, and 0.93 ± 0.02 eV for PN3, PN6 and PN9 (Fig. 5d), respectively, further verifying the enhanced kinetics of hydrogen oxidation reaction after the P–V shock.

In real applications, the thermal cycling stability of the perovskite electrode is an important parameter for solid oxide fuel cells. Hence, to investigate the thermal cycling stability of the treated LCTN, the system temperature monitored by a thermocouple was first increased from 650 to 800 °C and then

decreased to 650 °C (following the pattern of 650–800–650 °C) with an interval of 50 °C, and the R_p was collected at each temperature after stabilization. The results demonstrated that the polarization resistance changed slightly during the cycling measurement (Fig. 5e), suggesting the favorable thermal cycling stability of the treated LCTN. Moreover, no significant change in R_p was observed during the subsequent isothermal measurement (Fig. 5f).

Moreover, it was found that with increasing temperature, the electrical conductivity of all samples monotonously increased (Fig. 5g) and showed good cycling stability (Fig. S7). This was mainly associated with the generation of thermally activated charge carriers, resulting in an increase in carrier concentration. Furthermore, the order of electrical conductivity followed PN9 > PN6 > PN3 > pristine one. Compared to that of the pristine LCTN, the increased conductivity of PN3 was presumably because after the P–V shock, the exsolved metallic nickel nanoparticles possessing excellent conductivity could provide additional paths for electron conduction. Moreover, with an increase in the pulse number, more and more zero-valent nanoparticles were formed on the surface of the LCTN. For example, more paths could be built for electron conduction, resulting in an enhanced mobility of charge carriers and eventually yielding a more conductive LCTN. In addition, it could be expected that by generating zero-valent metal, the O 2p and T 3d (T signifies transition metals) orbits become more hybrid,[46] leading to an enhanced kinetics of electron transfer between T–O–T. Meanwhile, the additionally produced oxygen vacancies and the manipulated concentration of the TO Schottky defect due to the introduced A-site deficiency (Fig. S8) could accelerate the migration of oxygen anions. Synergistically, total conductivity was prominently enhanced after the P–V shock.

Additionally, the activation energy of conductivity was evaluated using the following equation:

$$\sigma = \frac{A}{T}\exp\left(-\frac{E_a}{kT}\right), \quad (7)$$

where A is the pre-exponential factor relating to the concentration and mobility of charge carriers, T is the temperature, E_a is the activation energy associated with the conducting process, and k is the Boltzmann constant. It was found that the pristine LCTN showed an activation energy of 1.02 ± 0.05 eV in the measured temperature range (Fig. S9), while lower E_a values of 0.93 ± 0.04, 0.82 ± 0.03 and 0.62 ± 0.03 eV were obtained for PN3, PN6 and PN9, respectively, further implying an enhanced kinetics of carrier mobility after P–V shock.

Cell performance of the P–V shocked LCTN

Cell performance was evaluated in a customized testing system consisting of a cell-supporting component, thermal couple, temperature remote controller and electrochemical workstation (Fig. S10). With respect to the pristine LCTN, it was found that the peak power density (PPD) changed between 0.01 and 0.06 W cm^{-2} in the temperature range of 650–800 °C (Fig. S11), suggesting an inferior electrochemical activity on oxidizing hydrogen molecules. In comparison with the pristine LCTN, it can be found that PN3 exhibited higher PPD values (0.12–0.32 W cm^{-2}) during the measurement (Fig. 6a), implying an enhanced kinetics of hydrogen oxidation reaction. This was mainly attributed to the generated metallic nickel nanoparticles that can dynamically break the H–H bond, thus facilitating the consumption of H_2 reactant.

Similarly, the PPD value increased prominently for PN6 and PN9 (Fig. 6b and c). For example, a promising PPD value of 1.11 W cm^{-2} was obtained for PN9 at 800 °C, which was improved by about 18.5 times compared to that of LCTN before P–V shock (Fig. 6e). Here, it is worth noting that lanthanum titanate-based perovskite usually shows unsatisfactory performance because of its intrinsically low activity. In other words, it has been experimentally demonstrated that P–V shock is an effective way to rapidly tailor the electrochemical performance of perovskites. In consideration of that, for an electrochemical reaction, electrons and ions are indispensable species; the enhancement of cell performance was presumably attributed to the increased oxygen vacancy concentration and the improved conducting ability, synergistically bringing about favorable activity. For example, in a unit time, more hydrogen molecules can be utilized for the P–V shocked LCTN, hence giving rise to a higher faradaic current density and power density during the operation. Moreover, during the subsequent 100 h test, there was no severe change in cell performance (Fig. 6d), suggesting a favorable stability of the treated perovskite.

In principle, the hydrogen oxidation reaction involves a series of procedures, such as gas diffusion, dissociative adsorption and charge transfer. To be more specific, driven by the gas concentration gradient (Δc) built between the environment and the fuel electrode, hydrogen molecules diffuse to the electrode surface; then, they are converted into adsorbed hydrogen ($H_{2,ads}$), realizing the procedure of gas–solid mass transfer. Through this step, the mass of the gas-phase reactant is transferred to the solid-phase electrode, which is important for a gas reaction that occurs on a solid's surface. Afterwards, catalyzed by the electrode catalyst, the H–H bond is dynamically broken to form H atoms (dissociation process). In fact, owing to the exsolved metallic Ni nanoparticles having good activity, the dissociative adsorption process can be efficiently improved. Subsequently, the generated H atoms spill over the nickel particle and migrate to the reacting zone (triple-phase boundary, Fig. S12) to react with the oxygen anion hopping from the counter side (Fig. 6f). By applying this step, the charge transfer is realized. After the P–V shock, the formed oxygen vacancies can offer more paths for oxygen anion hopping. Meanwhile, the formed charge carrier of e^- can efficiently flow away because of the generated metallic phase. Synergistically, in comparison with the LCTN before treatment, an enhanced kinetics of hydrogen oxidation reaction can be obtained for the treated LCTN, resulting in a lifted faradaic current. Finally, the formed water vapor leaves the electrode surface to reduce the system energy (Fig. S13).

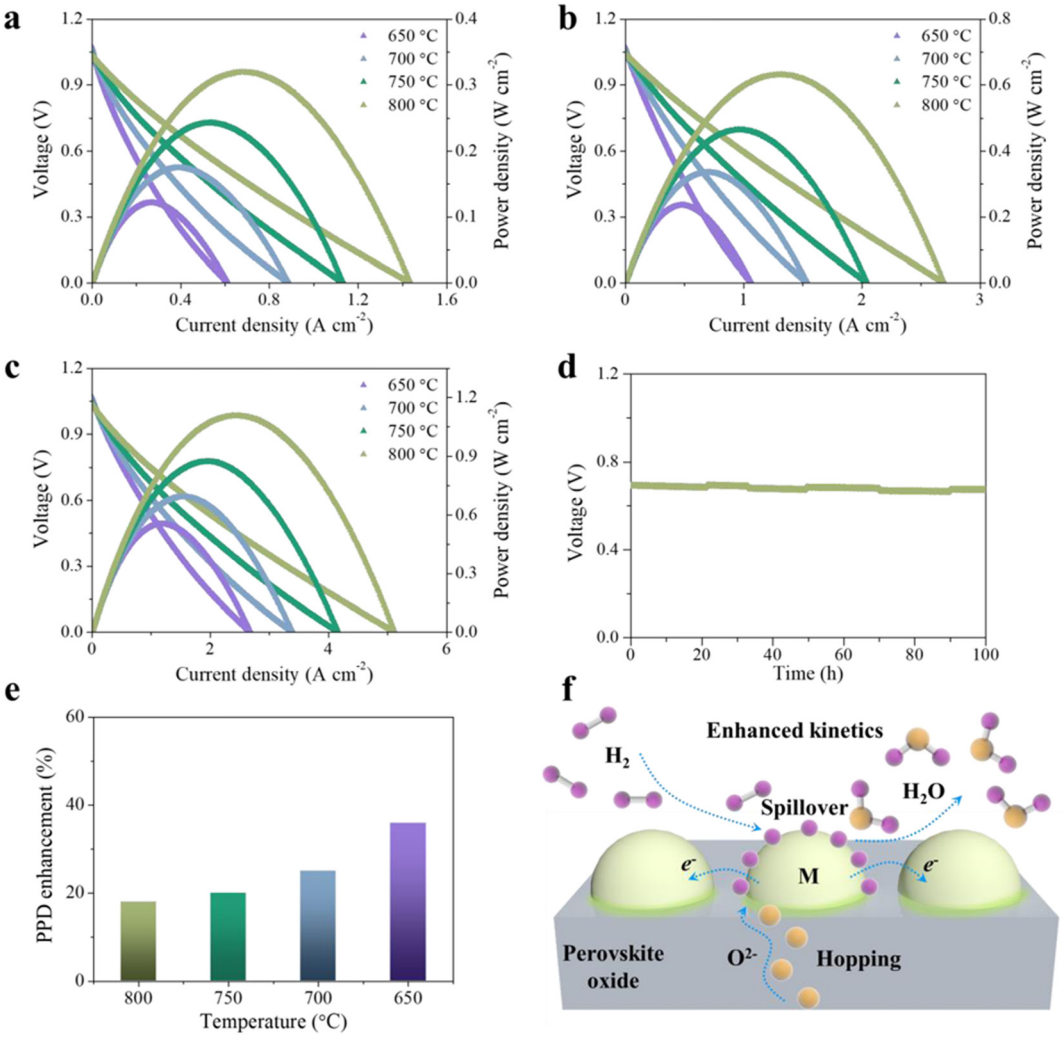

Fig. 6 *I–V(P)* curves of (a) PN3, (b) PN6 and (c) PN9 collected at different temperatures. (d) Galvanostatic measurement of PN9 at a current density of 1.2 A cm^{-2} at 800 °C. (e) Enhancement of the peak power density (PPD) of PN9 *versus* the pristine one at the measured temperatures. (f) Schematic of the enhanced electrocatalytic activity of the treated electrode on the hydrogen oxidation reaction.

Conclusions

In this study, we designed and demonstrated an approach to rapidly tailor the electrochemical activity of perovskites. We showed that by applying the P–V shock in a timescale of seconds, exsolution could be successfully triggered, and metallic Ni nanoparticles were formed on the surface of the perovskite support. With an increase in pulse number, the oxygen vacancy concentration increased first and then saturated after pulsing 9 times. Meanwhile, the particle density showed a similar variation trend with increasing pulse numbers. This was mainly because as the exsolution proceeded, the exsolvable transition metal atom in the perovskite lattice became less and less, resulting in a threshold of particle density. Moreover, owing to the additionally formed active sites for gas molecular adsorption and desorption and the channels for active species (such as oxygen anions and electrons) migration, improved electrochemical activity and enhanced kinetics of the hydrogen oxidation reaction were obtained. Consequently, a promising peak power density of 1.11 W cm^{-2} was obtained for PN9 at 800 °C. Compared to that of the pristine LCTN, the peak power density increased by ~18.5 times.

Methods

Material synthesis

$La_{0.32}Ca_{0.48}Ti_{0.94}Ni_{0.06}O_{3-\delta}$ perovskite was synthesized by applying a modified solid state reaction approach. High-purity lanthanum oxide, calcium carbonate, titanium dioxide, and nickel nitrate were used as raw materials. According to the stoichiometry, raw materials were carefully weighed by applying a high-precision balance, and the significant figures are read to four decimal places. After a pre-mixing of the weighed materials using an ultrasonic cell disruptor, the mixture was further mixed by a high-energy ball milling machine for 24 h

to ensure that the raw materials were fully in contact with each other, facilitating the following solid state reaction among the raw materials. Subsequently, two-step calcination (1100 °C 20 h and 1350 °C 20 h) was conducted on the precursor in an as-cleaned crucible.

Cell fabrication

To prepare the electrode ink, the as-synthesized LCTN powders were dispersed into a terpineol-based ink vehicle (fuel cell materials). The acquired slurry with proper viscosity was screen-printed (325 mesh) on one side of the $Zr_{0.92}Y_{0.08}O_{2-\delta}$ (8YSZ) electrolyte, followed by sintering at 1200 °C for 2 h. Then, $(La_{0.8}Sr_{0.2})_{0.95}MnO_3$-YSZ in a weight ratio of 1 : 1 ink was screen-printed on the opposite side of the electrolyte, which was then sintered at 1100 °C for 2 h. The fabricated cell was mounted on a customized ceramic tube using a high-temperature ceramic paste (Ceramabond 552). To avoid the influence of the current collector, gold mesh (Fiaxell) was applied as the current collector during the cell performance tests. For real-time temperature monitoring, a K-type thermocouple was fixed in the setup. After passing a water bubbler, the wet hydrogen with a flow rate of 50 mL min^{-1} was fed to the fuel side, and the other side was exposed to ambient air.

Characterization

The crystal structure of the as-prepared LCTN was investigated by applying an X-ray diffractometer of PANalytical X'Pert. Rietveld refinement was conducted using the HighScore Plus software package. High-resolution scanning electron microscopy (Zeiss Merlin) was used to collect information on the surface morphology. X-ray absorption near edge structure (XANES) was investigated in the Brookhaven National Laboratory (QAS beamline (7-BM) of the National Synchrotron Light Source II). Particle statistics were conducted using the commercial software Nano Measurer. The conductivity was measured by applying a four-probe method. Thermo Scientific iCAP 7000 was used to evaluate the composition of the as-prepared material. A high-speed camera (Miro M110) was applied to estimate the temperature of the thermal shock by fitting the ultraviolet-visible spectra. Simulations were carried out based on density functional theory and the Buckingham pair potential. For the ionic cycle, the convergence criterion was −0.03 eV $Å^{-1}$, while it was 10^{-6} eV for the electronic cycle. The iodometric titration approach was used to evaluate oxygen nonstoichiometry. A PARSTAT 4000 electrochemical workstation was employed to collect electrochemical impedance spectroscopy (10^5–10^{-1} Hz, 10 mV amplitude). To collect the *I–V* curves, the voltage was linearly swept from the OCV to 0 V.

Author contributions

Weiwei Fan: writing – original draft, review & editing, formal analysis, funding acquisition. Zhu Sun: investigation, data curation, writing – review & editing. Rui Xiao: writing – review & editing.

Conflicts of interest

The authors declare no competing interests.

Data availability

The data supporting this article have been included as part of the supplementary information (SI). Supplementary information is available. See DOI: https://doi.org/10.1039/d5nr05033b.

Acknowledgements

We acknowledge the funding from the National Key Research and Development Program of China (2024YFB4006704), the Natural Science Foundation of Jiangsu Province (BK20241316), the Jiangsu Province Carbon Peak and Carbon Neutrality Science and Technology Innovation Special Fund (BT2025012), the Innovative Research Group Project of the National Natural Science Foundation of China (52421003), the Start-up Research Fund of Southeast University (4003002330), the Provincial and Ministerial Level Key Laboratory Scientific Research (3203002403C3), the Chen Xing Plan of Shanghai Jiao Tong University, and the Shanghai Pilot Program for Basic Research Shanghai Jiao Tong University.

References

1 W. Bian, *et al.*, Revitalizing interface in protonic ceramic cells by acid etch, *Nature*, 2022, **604**, 479–485.
2 Y. Zhang, *et al.*, Thermal-expansion offset for high-performance fuel cell cathodes, *Nature*, 2021, **591**, 246–251.
3 R. J. H. Voorhoeve, D. W. Johnson, J. P. Remeika and P. K. Gallagher, Perovskite oxides: materials science in catalysis, *Science*, 1977, **195**, 827–833.
4 M. Papac, V. Stevanovi, A. Zakutayev and R. O'Hayre, Triple ionic-electronic conducting oxides for next-generation electrochemical devices, *Nat. Mater.*, 2021, **20**, 301–313.
5 J. T. S. Irvine, *et al.*, Evolution of the electrochemical interface in high-temperature fuel cells and electrolysers, *Nat. Energy*, 2016, **1**, 1–13.
6 B. Koo, *et al.*, Enhanced oxygen exchange of perovskite oxide surfaces through strain-driven chemical stabilization, *Energy Environ. Sci.*, 2018, **11**, 71–77.
7 W. J. Yin, *et al.*, Oxide perovskites, double perovskites and derivatives for electrocatalysis, photocatalysis, and photovoltaics, *Energy Environ. Sci.*, 2019, **12**, 442–462.
8 H. Y. Chen, *et al.*, Heterogeneous structure design for stable Li/Na metal batteries: Progress and prospects, *eScience*, 2025, **5**, 100281.
9 Y. Yang, *et al.*, A highly efficient bismuth substitution induced A-site ordered layered perovskite electrode for symmetrical solid oxide fuel cells, *J. Mater. Chem. A*, 2023, **11**, 7995–8002.

10 B. X. Li, J. T. S. Irvine, J. P. Ni and C. S. Ni, High-performance and durable alcohol-fueled symmetrical solid oxide fuel cell based on ferrite perovskite electrode, *Appl. Energy*, 2022, **306**, 118117.
11 F. He, *et al.*, A new Pd doped proton conducting perovskite oxide with multiple functionalities for efficient and stable power generation from ammonia at reduced temperatures, *Adv. Energy Mater.*, 2021, **11**, 2003916.
12 J. G. Lee, *et al.*, Replacement of Ca by Ni in a perovskite titanate to yield a novel perovskite exsolution architecture for oxygen–evolution reactions, *Adv. Energy Mater.*, 2020, **10**, 1903693.
13 C. C. Wang, Q. Yang, Y. Z. Ding, X. Y. Lu and D. Tian, Investigation of Ce-based buffer layers on electrochemical performance of YSZ-based symmetric solid oxide fuel cells, *Chem. Phys. Lett.*, 2024, **834**, 140981.
14 S. Kumar, A. Das and S. Omar, Electrochemical performance of $SrFeO_{3-\delta}$ for application as a symmetric electrode in solid oxide fuel cells, *ACS Appl. Energy Mater.*, 2023, **6**, 2049–2062.
15 G. S. Mtabazi and D. L. Samwel, Perspective and control of cation interdiffusion and interface reactions in solid oxide fuel cells (SOFCs), *J. Mater. Sci. Eng. B*, 2023, **292**, 116415.
16 K. J. Zhu, B. Luo, Z. H. Liu and X. Wen, Recent advances and prospects of symmetrical solid oxide fuel cells, *Ceram. Int.*, 2022, **48**, 8972–8986.
17 Z. Zakaria, S. H. Hassan, N. Shaari, A. Z. Yahaya and Y. B. Kar, A review on recent status and challenges of yttria stabilized zirconia modification to lowering the temperature of solid oxide fuel cells operation, *Int. J. Energy Res.*, 2020, **44**, 631–650.
18 Y. Choi, *et al.*, Unravelling inherent electrocatalysis of mixed-conducting oxide activated by metal nanoparticle for fuel cell electrodes, *Nat. Nanotechnol.*, 2019, **14**, 245–251.
19 Z. Zhao, *et al.*, Graphene-nanopocket-encaged PtCo nanocatalysts for highly durable fuel cell operation under demanding ultralow-Pt-loading conditions, *Nat. Nanotechnol.*, 2022, **17**, 968–975.
20 D. Zhang, *et al.*, Potential reduction-induced fast exsolution of hyperfine nanoparticles afford highly active CO_2 reduction reaction, *Appl. Catal., B*, 2026, **382**, 125937.
21 Y. T. Jiang, *et al.*, Coupling lattice strain and sulfur vacancy in tin monosulfide/reduced graphene oxide composite for high–performance sodium–ion storage, *Energy Environ. Mater.*, 2025, **8**, 12891.
22 R. L. Li, *et al.*, SnS_2 nanoparticles embedded in sulfurized polyacrylonitrile composite fibers for high–performance potassium–ion batteries, *Interdiscip. Mater.*, 2024, **3**, 150–159.
23 B. Zhang and Y. Qin, Interface tailoring of heterogeneous catalysts by atomic layer deposition, *ACS Catal.*, 2018, **8**, 10064–10081.
24 K. Develos-Bagarinao, T. Ishiyama, H. Kishimoto, H. Shimada and K. Yamaji, Nanoengineering of cathode layers for solid oxide fuel cells to achieve superior power densities, *Nat. Commun.*, 2021, **12**, 1–12.
25 D. Ding, X. X. Li, S. Y. Lai, K. Gerdes and M. L. Liu, Enhancing SOFC cathode performance by surface modification through infiltration, *Energy Environ. Sci.*, 2014, **7**, 552–575.
26 S. P. Jiang, Nanoscale and nano-structured electrodes of solid oxide fuel cells by infiltration: Advances and challenges, *Int. J. Hydrogen Energy*, 2012, **37**, 449–470.
27 J. M. Vohs and R. J. Gorte, High-performance SOFC cathodes prepared by infiltration, *Adv. Mater.*, 2009, **21**, 943–956.
28 Y. Gao, *et al.*, Energetics of nanoparticle exsolution from perovskite oxides, *J. Phys. Chem. Lett.*, 2018, **9**, 3772–3778.
29 H. Arandiyan, *et al.*, In situ exsolution of bimetallic Rh-Ni nanoalloys: a highly efficient catalyst for CO_2 methanation, *ACS Appl. Mater. Interfaces*, 2018, **10**, 16352–16357.
30 Y. Gao, J. Wang, Y. Q. Lyu, K. Lam and F. Ciucci, In situ growth of Pt_3Ni nanoparticles on an A-site deficient perovskite with enhanced activity for the oxygen reduction reaction, *J. Mater. Chem. A*, 2017, **5**, 6399–6404.
31 D. Neagu, G. Tsekouras, D. N. Miller, H. Menard and J. T. S. Irvine, In situ growth of nanoparticles through control of non-stoichiometry, *Nat. Chem.*, 2013, **5**, 916–923.
32 Y. Luo, *et al.*, Unraveling the evolution and regulation mechanisms of reversible exsolution in perovskite–based nanoparticles, *Adv. Funct. Mater.*, 2025, 17547.
33 L. Sánchez de Bustamante, *et al.*, Dual doping synergy: Optimizing $SrMoO_3$ perovskite anodes via *in situ* Ni exsolution and Cr doping for enhanced SOFC efficiency, *J. Alloys Compd.*, 2025, **1018**, 179116.
34 J. Bai, *et al.*, Triphenylphosphine–assisted exsolution engineering on Ruddlesden–Popper perovskites for promoting oxygen evolution, *Energy Environ. Mater.*, 2023, **7**, 12668.
35 R. Zhou, Y. Y. Gu, H. L. Dai, Y. S. Xu and L. Bi, *In situ* exsolution of PrO_{2-x} nanoparticles boost the performance of traditional $Pr_{0.5}Sr_{0.5}MnO_{3-\delta}$ cathode for proton-conducting solid oxide fuel cells, *J. Eur. Ceram. Soc.*, 2023, **43**, 6612–6621.
36 J. Guo, *et al.*, Low-temperature exsolution of Ni-Ru bimetallic nanoparticles from A-dite deficient double perovskites, *Small*, 2022, **18**, 2107020.
37 M. Kothari, *et al.*, Platinum incorporation into titanate perovskites to deliver emergent active and stable platinum nanoparticles, *Nat. Chem.*, 2021, **13**, 677–682.
38 Y. Luo, *et al.*, Precise regulation of in situ exsolution components of nanoparticles for constructing active interfaces toward carbon dioxide reduction, *ACS Nano*, 2025, **19**, 1463–1477.
39 W. W. Fan, Z. Sun, Y. Bai, K. Wu and Y. H. Cheng, Highly stable and efficient perovskite ferrite electrode for symmetrical solid oxide fuel cells, *ACS Appl. Mater. Interfaces*, 2019, **11**, 23168–23179.
40 Y. F. Sun, *et al.*, A-site-deficiency facilitated in situ growth of bimetallic Ni-Fe nano-alloys: a novel coking-tolerant fuel cell anode catalyst, *Nanoscale*, 2015, **7**, 11173–11181.
41 T. L. Zhu, *et al.*, Exsolution and electrochemistry in perovskite solid oxide fuel cell anodes: Role of stoichiometry in Sr(Ti,Fe,Ni)O_3, *J. Power Sources*, 2019, **439**, 227077.
42 E. Wahlstrom, *et al.*, Bonding of gold nanoclusters to oxygen vacancies on rutile TiO_2 (110), *Phys. Rev. Lett.*, 2003, **90**, 026101–026105.

43 S. B. Liu, Q. X. Liu and J. L. Luo, Highly stable and efficient catalyst with in situ exsolved Fe-Ni alloy nanospheres socketed on an oxygen deficient perovskite for direct CO_2 electrolysis, *ACS Catal.*, 2016, **6**, 6219–6228.
44 J. Y. Wang, *et al.*, Tuning point defects by elastic strain modulates nanoparticle exsolution on perovskite oxides, *Chem. Mater.*, 2021, **33**, 5021–5034.
45 Y. Gao, D. J. Chen, M. Saccoccio, Z. H. Lu and F. Ciucci, From material design to mechanism study: Nanoscale Ni exsolution on a highly active A-site deficient anode material for solid oxide fuel cells, *Nano Energy*, 2016, **27**, 499–508.
46 L. De Rogatis, *et al.*, Embedded phases: a way to active and stable catalysts, *ChemSusChem*, 2010, **3**, 24–42.